Journal of Corrosion and Materials *J. Corros. Mater.* (2026) 5(2), 196–210.
www.corromat.com

Radiative Mixed-Convection Transport of Cu–Al_2O_3/Water Hybrid Nanofluid over a Convectively Heated Vertical Riga Plate

Lino de Oliveira Santos[1,*]

Department of Chemical Engineering, University of Coimbra–Pólo II, 3030-790 Coimbra, Portugal

[*]Corresponding author: lino@eq.uc.pt

(Received: 25 July 2026. Received in revised form: 30 September 2026. Accepted: 14 October 2026. Published online: 30 December 2026.)

Abstract

The unsteady stagnation-point mixed-convection flow of a Cu–Al_2O_3/water hybrid nanofluid past a stationary vertical Riga plate is analyzed in the presence of convective boundary heating and Rosseland thermal radiation. The wall-fixed configuration of Riga plate is modeled using periodic distribution of electrodes and magnets that yield a parallel wall Lorentz force via an exponentially decaying Grinberg term. The externally prescribed velocity is $u_e(x,t) = ax/(1-ct)$, while the convective wall heat flux specification involves the Biot number. The description of hybrid nanofluid includes uniform nanoparticle concentrations, $\phi_{\mathrm{Cu}} = \phi_{\mathrm{Al_2O_3}} = 0.02$, where water acts as base fluid. With the aid of similarity transformations, the system of nonlinear partial differential equations is cast in the form of coupled nonlinear ordinary differential equations. The solution of nonlinear boundary value problem is obtained via a fourth-order collocation approach, whereas stability analysis using temporal eigenvalues differentiates between stable and unstable solutions. For the limit case of viscous fluid flow, $Re_x^{1/2}C_f = 1.2325876$ and $Re_x^{-1/2}Nu_x = 0.045466$, 0.083373, and 0.142974 for $Bi = 0.05$, 0.10, and 0.20, respectively. The existence of dual branches is reported when the mixed convection is opposing while there is only a single branch when the mixed convection is assisting. The least negative eigenvalues confirm that the first branch is stable while the second one is unstable. Higher deceleration in the time-dependent unsteady motion leads to a lower wall shear and enhanced heat transfer rate. Larger electromagnetic parameters enhance heat transfer owing to electromagnetic acceleration while increasing skin friction due to Lorentz-force effect. Larger decay parameter leads to less Lorentz-force effect thereby reducing shear and heat transfer. The findings reveal the contributions of unsteadiness, buoyancy, convection, radiation, and localized electromagnetic force in ensuring the stable flow of Cu-Al_2O_3/Water hybrid nanofluid along the wall.

Keywords: Cu–Al_2O_3/water hybrid nanofluid; Riga plate; mixed convection; Rosseland radiation; convective heating; dual solutions; temporal stability; wall heat transfer.

1. Introduction

Nanofluids consist of nanoscale particles dispersed into a working liquid to augment the thermophysical behavior of the base liquid [1]. Initial conductivity studies of metallic particle suspensions revealed significant enhancements over the base liquid conductivity [2]. Buongiorno's transport model related nanoparticle volume fraction to Brownian diffusion, thermophoresis, and boundary-layer heat transfer [3]. The Tiwari–Das formulation provided another influential model by introducing solid-volume-fraction effects into nanofluid heat transfer [4]. Literature reviews of convective nanofluid transport have noted that thermal improvement is coupled with viscosity increase, density augmentation, heat-capacity change, and pressure drop [5]. Recent modelling reviews further confirm that heat-transfer augmentation should be analyzed together with hydrodynamic resistance [6].

In a hybrid nanofluid, two solid-phase nanoparticles are suspended in a base liquid. Hybrid composition is useful when one type of nanoparticle cannot simultaneously achieve heat transfer enhancement, thermal stability, and reasonable viscosity. Metals generally exhibit good conductivity enhancement, whereas ceramics are known for their robustness at high temperatures. Hybrid nanofluid reviews identify nanoparticle pair, volume fraction, conductivity ratio, and viscosity closure as major variables [7]. Further review work confirms that the heat-transfer response depends on the selected hybrid combination and flow configuration [8]. State-of-the-art analysis also shows that hybrid nanofluids must be evaluated through both thermal and hydrodynamic effects [9]. For instance, Cu–Al_2O_3/water is a metallic-ceramic pair since the former exhibits excellent conductivity and the latter provides robustness in a high-heat-capacity base liquid. Experimental work on Al_2O_3-Cu/water suspensions confirmed that hybridization can improve thermophysical behavior [10]. Computational enclosure studies also reported heat-transfer enhancement through hybrid nanofluid use [11]. Numerical work on hydromagnetic hybrid transport further demonstrated the importance of analyzing boundary-layer conditions together with nanoparticle composition [12].

Material contrasts are notable in the Cu–Al_2O_3/water suspension. The material properties of copper, alumina, and water are presented in Table 1; hence, the selected volume fractions of $\phi_{\mathrm{Cu}} = \phi_{\mathrm{Al_2O_3}} = 0.02$ indicate that the system will have material contrasts since the high-conductivity copper material will oppose the other two with relatively low conductivities. As such, the hybrid nanofluid conductivity gain from copper is counteracted by the increased viscosity and inertia from nanoparticle loading.

Another transport phenomenon that controls wall transfer in a vertical boundary layer is the presence of buoyancy. Mixed convection occurs when the flow is driven by both pressure and buoyancy forces, whereas pure convection can be either helping or resisting to the pressure-driven motion. Classical boundary-layer analysis showed that reverse-flow and separation-related behavior can arise in such transport settings [13]. Mixed-convection studies in porous media also demonstrated that multiple solutions may occur under certain flow conditions [14]. Later boundary-layer work confirmed that stable solution branches must be distinguished from mathematically possible branches [15]. The same point is critical for the analysis of Riga plate hybrid nanofluid flow since numerical existence of a lower branch of a multiple solution set does not ensure its physical realizability.

Riga plates introduce electromagnetic force in the boundary layer near a surface through a periodic array of electrodes and permanent magnets. The force created by the electrodes and magnets interacts with one another to give rise to a wall-parallel Lorentz force that vanishes exponentially with wall-normal distance from the wall. This is in contrast to constant magnetization force fields since the Lorentz force generated by the Riga effect is concentrated in the wall region. The idea behind the Riga plate has been proposed in previous studies [16], whereas the exponentially decreasing potential-force model can be attributed to Grinberg [17]. Free-convection analysis over a Riga plate showed how the localized electromagnetic force modifies near-wall transport [18]. Mixed-convection analysis further confirmed that aiding and opposing Riga-plate flows respond differently to electromagnetic forcing [19].

Studies analyzing Riga plate transport include nanofluid and hybrid nanofluid effects, thermal radiation, hydrodynamic slip, convective wall heating, and temporal stability considerations. Thermal radiation and electromagnetohydrodynamic effects on viscous nanofluid flow over a Riga plate have been studied by Bhatti et al. [20]. Effects of slip conditions for mixed convection of nanofluid over a horizontal Riga plate were performed by Ayub et al. [21]. Heat transfer enhancement due to buoyancy-driven nanofluid flow over a convectively heated vertical Riga plate has been carried out by Ahmad *et al.* [22]. The occurrence of multiple solutions in mixed-convection flow of Cu–Al_2O_3/water hybrid nanofluid over a vertical Riga plate is investigated by Khashiie et al. [23]. Unsteady hybrid nanofluid transport toward a Riga plate in stagnation flow has also been examined [24]. EMHD radiating fluid flow along a vertical Riga plate with suction in a rotating system has been considered as another related configuration [25]. Radiation effects on Cu–Al_2O_3/water transport toward an EMHD plate have been reported [26]. Slip and thermal radiation effects on shrinking Riga plates have also been analyzed [27]. Carreau–Yasuda hybrid nanofluid flow over a convectively heated Riga surface in stagnation flow has been studied in a later computational assessment [28].

Many heat exchange surfaces do not maintain a constant temperature at their boundaries; rather, they exchange heat with an adjacent fluid and establish a certain temperature that is dependent on heat transfer coefficient and the adjacent fluid. Biot number is a measure of wall transport with respect to the surrounding environment. Stagnation-point flow analysis of convection over a convectively heated wall reveals the simultaneous influence of temperature and flow on wall temperature and heat transfer coefficient [29]. Related stagnation-point work with convective boundary conditions and partial velocity slip further confirms the importance of wall thermal interaction [30]. In the current configuration, the same wall is exposed to no-slip velocity field, localized Lorentz force, and heat transfer with respect to a heating medium. Wall derivatives of velocity and temperature are therefore affected by both momentum and thermal interactions in the flow field.

Radiation effects are accounted for using the Rosseland approximation to allow for heat transfer across radiative surfaces and fluids. Rosseland's model expresses radiative flux through a temperature gradient relation [31]. Through linearization of T^4, radiative term appears in the energy equation as a thermal diffusive term. The radiative diffusivity term acts in collaboration with hybrid nanofluid conductivity term to determine heat transfer rate. Heat transfer rate therefore depends on a combined multiplier consisting of k_{hnf}/k_{H_2O} and radiation parameter R.

Multiple solution analysis is employed in the investigation of thermal properties of Cu–Al_2O_3/water hybrid nanofluid flow with unsteadiness, electromagnetohydrodynamics, thermal radiation, and convective heating in stagnation flow. Skin friction coefficient, Nusselt number, profiles of velocity and temperature, multiple solution structure, and the sign of the first eigenvalue are the quantities of interest in this study. The focus in the discussion will be the lower stable branch since although the upper branch satisfies the same physical boundary conditions, it turns out to be unstable to small disturbances.

The impact of a given parameter on shear and heat transfer needs to be examined separately since the same physical parameter may affect each transport differently. Skin friction depends on velocity derivative and correction terms for viscosity, whereas Nusselt number is sensitive to temperature derivatives and combined thermal diffusive effect. If a

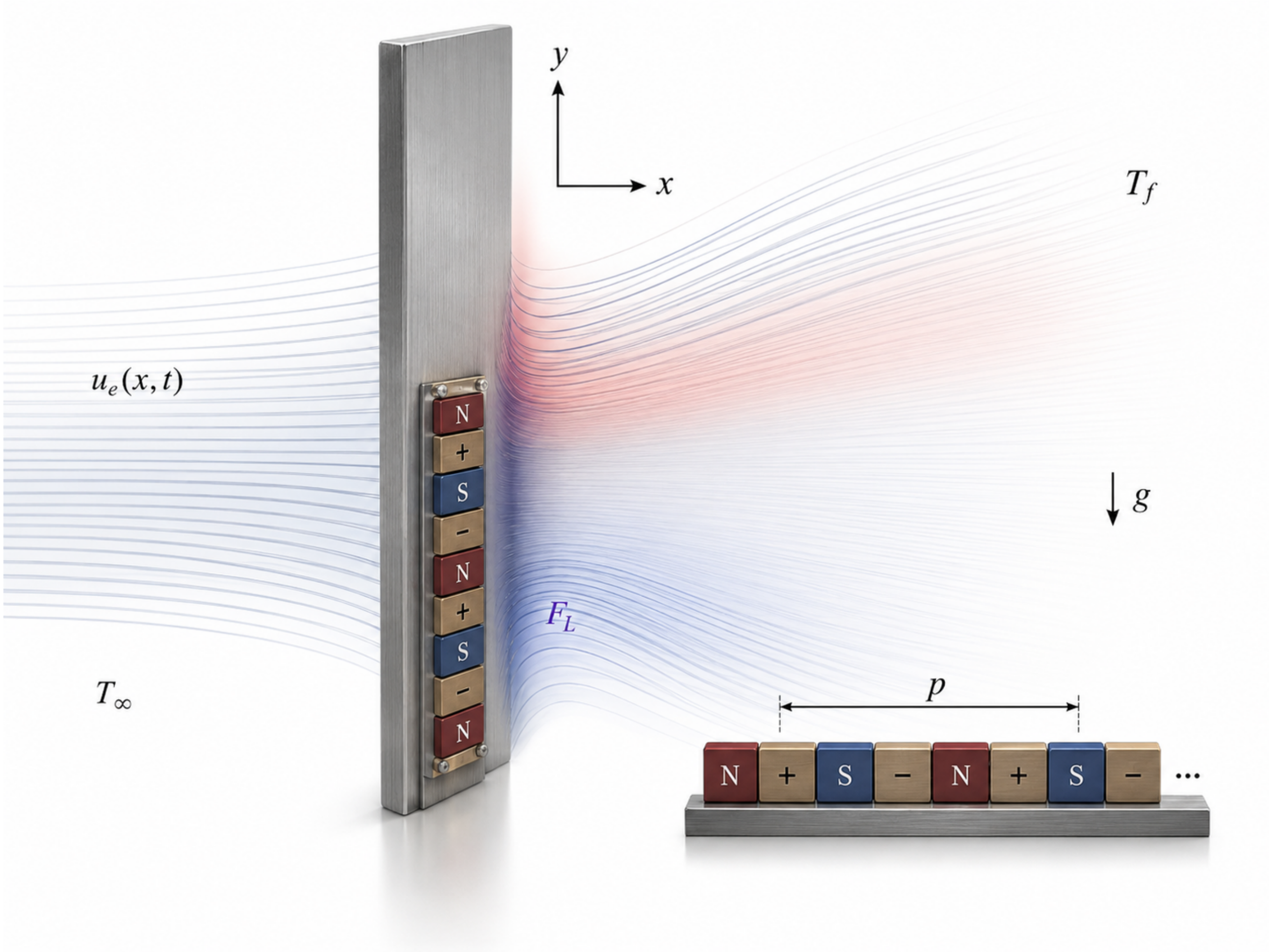

Figure 1: Riga-actuated vertical boundary layer.

parameter increases near-wall momentum, it will raise velocity gradient at the wall and heat transfer rate as well. On the other hand, parameters affecting temperature directly will raise wall temperature regardless of velocity field. The results reported below will rely on plots of gradients together with velocity and temperature profiles in order to associate each parameter with a specific transport quantity.

Eigenvalues of the first and second solution branches are computed separately to identify unstable solutions among the multiple solutions. Since temporal stability requires eigenvalues with positive real part, a negative sign indicates instability. A multiple solution set having both eigenvalues positive is physically impossible since a small perturbation causes exponential growth, rendering the solution non-stationary. Hence, in spite of showing lower skin friction coefficient and Nusselt number, an unstable solution is disregarded in the discussion.

2. Physical configuration and governing equations

A fixed vertical Riga plate immersed in an incompressible Cu–Al_2O_3/water hybrid nanofluid is assumed in this study. Streamwise and wall-normal directions are defined by coordinates x and y, respectively, such that the fluid occupies $y \geq 0$. The external stagnation velocity is taken to be of the form

$$u_e(x,t) = \frac{ax}{1-ct}, \tag{1}$$

with constant parameters $a > 0$ and c. Eq. (1) ensures that the stagnation velocity is linear with respect to streamwise coordinate x and temporally varying.

The surface is convectively heated with an external medium of temperature $T_f(x,t)$, and ambient hybrid nanofluid temperature is taken to be T_∞. Wall conditions are no-penetration and no-slip. Lorentz force is produced by electrodes and permanent magnets placed periodically on the surface, causing exponentially decaying wall-parallel Lorentz force with increasing wall-normal distance. Figure 1 illustrates the setup of physical domain and coordinate system.

The radiative heat flux is described by the expression

$$q_r = -\frac{4\sigma^*}{3k^*}\frac{\partial T^4}{\partial y}, \tag{2}$$

Table 1: Constants related to the thermophysical properties of Cu–Al_2O_3/water.

Material	ρ (kg m^{-3})	C_p (J kg^{-1}K^{-1})	k (W m^{-1}K^{-1})
Cu	8933	385	400
Al_2O_3	3970	765	40
H_2O	997.1	4179	0.613

where σ^* is the Stefan-Boltzmann constant and k^* is the mean absorption coefficient. Its linearization about the ambient temperature yields

$$T^4 \simeq 4T_\infty^3 T - 3T_\infty^4, \tag{3}$$

and thus

$$q_r = -\frac{16\sigma^* T_\infty^3}{3k^*}\frac{\partial T}{\partial y}. \tag{4}$$

Consequently, the radiation term increases thermal diffusion in the energy equation.

The boundary-layer equations are

$$\frac{\partial u}{\partial x} + \frac{\partial v}{\partial y} = 0, \tag{5}$$

$$\frac{\partial u}{\partial t} + u\frac{\partial u}{\partial x} + v\frac{\partial u}{\partial y} = \frac{\partial u_e}{\partial t} + u_e\frac{\partial u_e}{\partial x} + \frac{\mu_{hnf}}{\rho_{hnf}}\frac{\partial^2 u}{\partial y^2} + \frac{\pi j_0 M_0(x,t)}{8\rho_{hnf}}\exp\left(-\frac{\pi y}{p}\right) + \beta_{hnf} g(T - T_\infty), \tag{6}$$

$$\frac{\partial T}{\partial t} + u\frac{\partial T}{\partial x} + v\frac{\partial T}{\partial y} = \frac{1}{(\rho C_p)_{hnf}}\left(k_{hnf} + \frac{16\sigma^* T_\infty^3}{3k^*}\right)\frac{\partial^2 T}{\partial y^2}. \tag{7}$$

Mass conservation is expressed by Eq. (5). The momentum equation (6) includes local acceleration, convective acceleration, free-stream straining, viscous diffusion, exponentially decaying electromagnetic force, and buoyancy. The energy equation (7) accounts for conductive and radiative diffusion of thermal energy in the hybrid nanofluid.

The boundary conditions are

$$v = 0, \qquad u = 0, \qquad -k_{hnf}\frac{\partial T}{\partial y} = h_f(T_f - T) \quad \text{at } y = 0, \tag{8}$$

$$u \to u_e(x,t), \qquad T \to T_\infty \quad \text{as } y \to \infty. \tag{9}$$

The thermal condition in Eq. (8) permits the wall temperature to vary depending on the heat-transfer coefficient between the wall and fluid h_f.

3. Hybrid nanofluid properties

The formulas for the viscosity, density, heat capacity product, and thermal expansion term are as follows:

$$\mu_{hnf} = \mu_{H_2O}(1 - \phi_{\mathrm{Al_2O_3}} - \phi_{\mathrm{Cu}})^{-2.5}, \tag{10}$$

$$\rho_{hnf} = \phi_{\mathrm{Al_2O_3}}\rho_{\mathrm{Al_2O_3}} + \phi_{\mathrm{Cu}}\rho_{\mathrm{Cu}} + (1 - \phi_{hnf})\rho_{H_2O}, \tag{11}$$

$$(\rho C_p)_{hnf} = \phi_{\mathrm{Al_2O_3}}(\rho C_p)_{\mathrm{Al_2O_3}} + \phi_{\mathrm{Cu}}(\rho C_p)_{\mathrm{Cu}} + (1 - \phi_{hnf})(\rho C_p)_{H_2O}, \tag{12}$$

$$(\rho\beta)_{hnf} = (1 - \phi_{hnf})(\rho\beta)_{H_2O} + \phi_{\mathrm{Al_2O_3}}(\rho\beta)_{\mathrm{Al_2O_3}} + \phi_{\mathrm{Cu}}(\rho\beta)_{\mathrm{Cu}}, \tag{13}$$

where $\phi_{hnf} = \phi_{\mathrm{Al_2O_3}} + \phi_{\mathrm{Cu}}$. As can be seen from the formulas above, nanoparticle introduction results in modification of momentum diffusion, inertia, thermal diffusion, and buoyancy simultaneously.

The expression for thermal conductivity ratio of the hybrid nanofluid is

$$\frac{k_{hnf}}{k_{H_2O}} = \frac{\dfrac{\phi_{\mathrm{Al_2O_3}}k_{\mathrm{Al_2O_3}} + \phi_{\mathrm{Cu}}k_{\mathrm{Cu}}}{\phi_{\mathrm{Al_2O_3}} + \phi_{\mathrm{Cu}}} + 2k_{H_2O} + 2(\phi_{\mathrm{Al_2O_3}}k_{\mathrm{Al_2O_3}} + \phi_{\mathrm{Cu}}k_{\mathrm{Cu}}) - 2(\phi_{\mathrm{Al_2O_3}} + \phi_{\mathrm{Cu}})k_{H_2O}}{\dfrac{\phi_{\mathrm{Al_2O_3}}k_{\mathrm{Al_2O_3}} + \phi_{\mathrm{Cu}}k_{\mathrm{Cu}}}{\phi_{\mathrm{Al_2O_3}} + \phi_{\mathrm{Cu}}} + 2k_{H_2O} - (\phi_{\mathrm{Al_2O_3}}k_{\mathrm{Al_2O_3}} + \phi_{\mathrm{Cu}}k_{\mathrm{Cu}}) + (\phi_{\mathrm{Al_2O_3}} + \phi_{\mathrm{Cu}})k_{H_2O}}. \tag{14}$$

Since the thermal conductivity of copper is considerably larger than that of water and alumina, the copper fraction significantly affects k_{hnf}. It should be assessed taking into account modifications to other effective material properties.

From Table 1, it can be seen that Cu-Al_2O_3/water represents a mixture of a metallic phase (Cu), a ceramic phase (Al_2O_3), and an aqueous medium (H_2O). Such material combination justifies why the analysis must consider the velocity and temperature fields simultaneously; namely, because thermal conductivity alone cannot be used for wall heat transfer estimation.

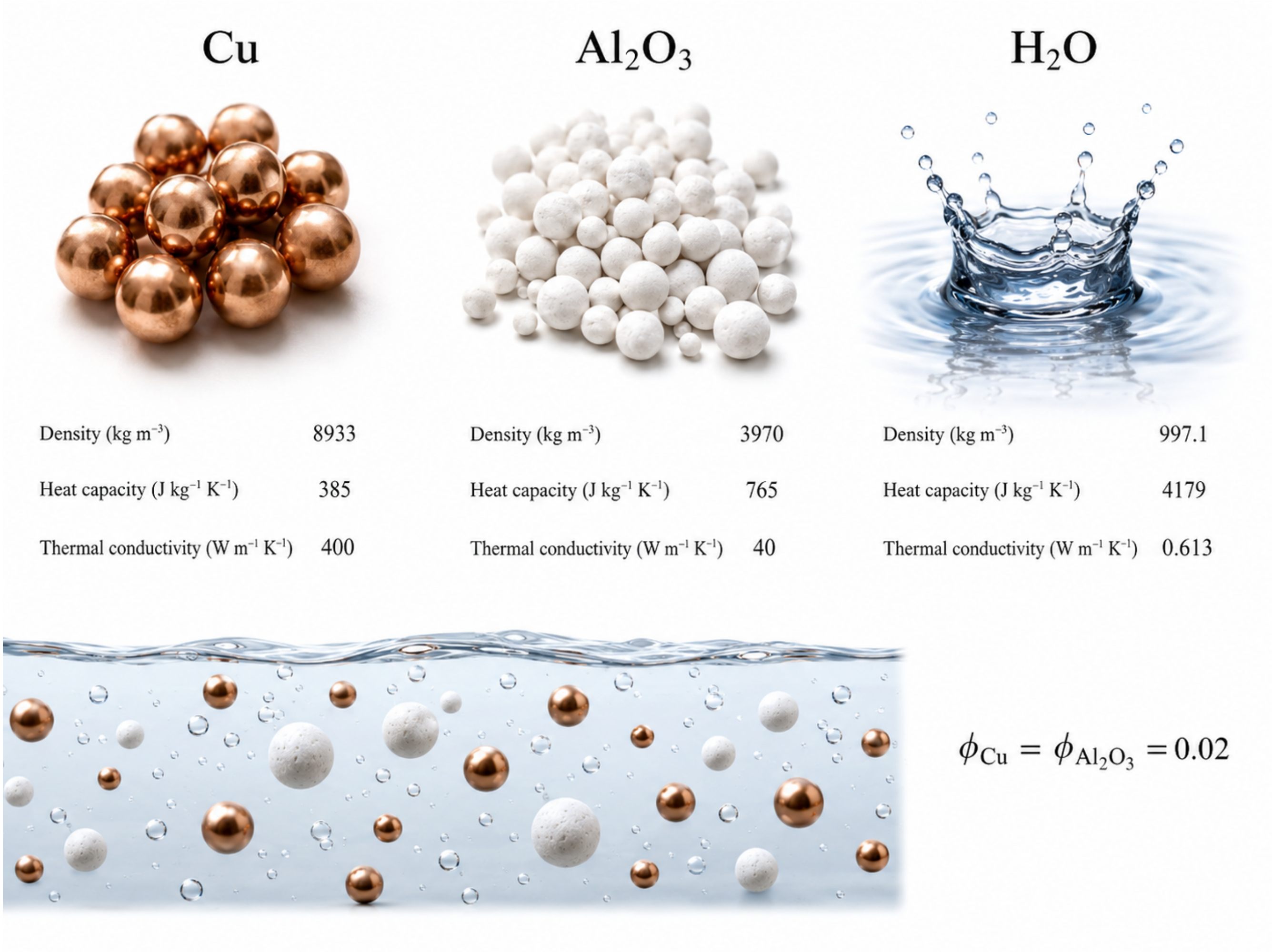

Figure 2: Thermal material contrast in the hybrid suspension.

Figure 2 demonstrates the material contrast implied in the Cu-Al_2O_3/water hybrid suspension. The metallic phase has a high thermal conductivity, the aqueous medium has the largest heat capacity, and the ceramic phase has intermediate characteristics. For the equal volume fractions of 2% of each material, copper is the metallic phase, alumina is the ceramic phase, and water is the aqueous medium.

4. Similarity reduction and wall quantities

To derive similarity, we use the following expressions:

$$u = \frac{ax}{1-ct} f'(\eta), \qquad v = -\left(\frac{a\nu_{H_2O}}{1-ct}\right)^{1/2} f(\eta), \tag{15}$$

$$\theta(\eta) = \frac{T - T_\infty}{T_f(x,t) - T_\infty}, \qquad \eta = y\left(\frac{a}{\nu_{H_2O}(1-ct)}\right)^{1/2}. \tag{16}$$

The introduced functions satisfy Eq. (5) and the similarity transformation normalizes the velocity and temperature fields in terms of the local external strain and wall-fluid temperature difference.

For similarity reduction, it is necessary to transform the time-dependent quantities:

$$M_0(x,t) = \frac{(x/l)M_0}{(1-ct)^2}, \qquad \tilde{b}(t) = (1-ct)^{-1/2} b, \qquad \tilde{h}_f(t) = (1-ct)^{-1/2} h_f. \tag{17}$$

These formulas permit introducing the common wall-normal scale that satisfies the required similarity transformation of the electromagnetic forcing and heat transfer coefficients.

Substitution of Eqs. (15)–(17) into Eqs. (6) and (7) yields the following ordinary differential equations:

$$\frac{\mu_{hnf}/\mu_{H_2O}}{\rho_{hnf}/\rho_{H_2O}} f''' + ff'' - (f')^2 + 1 + A\left(1 - f' - \frac{\eta}{2} f''\right) + \frac{\rho_{H_2O}}{\rho_{hnf}} Z e^{-b\eta} + \frac{\beta_{hnf}}{\beta_{H_2O}} \lambda\theta = 0, \tag{18}$$

$$\frac{1}{Pr}\frac{(\rho C_p)_{H_2O}}{(\rho C_p)_{hnf}}\left(\frac{k_{hnf}}{k_{H_2O}}+\frac{4R}{3}\right)\theta''+f\theta'-\frac{A}{2}\eta\theta'=0. \tag{19}$$

The corresponding transformed boundary conditions are

$$f(0)=0, \qquad f'(0)=0, \qquad \theta'(0)=-\frac{k_{H_2O}}{k_{hnf}}Bi[1-\theta(0)],$$
$$f'(\eta)\to 1, \qquad \theta(\eta)\to 0 \qquad \text{as } \eta\to\infty. \tag{20}$$

Eqs. (18) and (19) include viscous diffusion, stagnation point convection, unsteadiness, localized acceleration due to Lorentz force, and buoyancy. Eq. (19) includes effective thermal diffusion, thermal radiation, and convection due to flow.

Dimensionless parameters include Prandtl number

$$Pr=\frac{(\mu C_p)_{H_2O}}{k_{H_2O}}, \tag{21}$$

the parameter measuring electromagnetic influence on flow

$$Z=\frac{\pi j_0 M_0}{8a^2 l\rho_{H_2O}}, \tag{22}$$

decay rate

$$b=\frac{\pi}{p}\left(\frac{\nu_{H_2O}}{a}\right)^{1/2}, \tag{23}$$

unsteadiness

$$A=\frac{c}{a}, \tag{24}$$

radiative diffusion

$$R=\frac{4\sigma^* T_\infty^3}{k_{H_2O}k^*}, \tag{25}$$

dimensionless gravitational buoyancy

$$\lambda=\frac{Gr_x}{Re_x^2}, \tag{26}$$

and convective wall heating parameter

$$Bi=\frac{h_f}{k_{H_2O}}\left(\frac{\nu_{H_2O}}{a}\right)^{1/2}. \tag{27}$$

Here, the Grashof and Reynolds numbers are defined as follows:

$$Gr_x=\frac{g\beta_{H_2O}[T_f(x,t)-T_\infty]x^3}{\nu_{H_2O}^2}, \qquad Re_x=\frac{u_e(x,t)x}{\nu_{H_2O}}. \tag{28}$$

In particular, Z quantifies the intensity of Lorentz forces, b specifies their decay rate, A measures the influence of unsteadiness, R quantifies radiative diffusion, λ characterizes the relative magnitudes of gravitational and forced flows, and Bi quantifies the intensity of wall heating.

Local skin friction is

$$C_f=\frac{\mu_{hnf}}{\rho_{H_2O}u_e^2(x,t)}\left.\frac{\partial u}{\partial y}\right|_{y=0}, \tag{29}$$

while the local Nusselt number is

$$Nu_x=-\frac{x}{k_{H_2O}[T_f-T_\infty]}\left[\left(k_{hnf}\frac{\partial T}{\partial y}\right)+\left.(q_r)\right|_{y=0}\right]. \tag{30}$$

Reduced expressions for skin friction and Nusselt numbers are given by

$$Re_x^{1/2}C_f=\frac{\mu_{hnf}}{\mu_{H_2O}}f''(0), \qquad Re_x^{-1/2}Nu_x=\left(\frac{k_{hnf}}{k_{H_2O}}+\frac{4R}{3}\right)[-\theta'(0)]. \tag{31}$$

In particular, the wall shear is determined by $f''(0)$ with the viscosity adjustment factor μ_{hnf}/μ_{H_2O}, while wall heat flux is determined by $-\theta'(0)$ with the adjustment factors for conduction and radiation.

Figure 3 depicts the overall workflow leading from boundary-layer functions to similarity solution functions, collocation grid construction, and eigenvalue-based stability analysis. Top figures illustrate the mapping of wall functions onto the vertical coordinate. Middle panels illustrate the similarity functions alongside Lorentz contributions and normalization. Lower panels illustrate the domain for collocation and the sign criteria for selecting the physically correct branch.

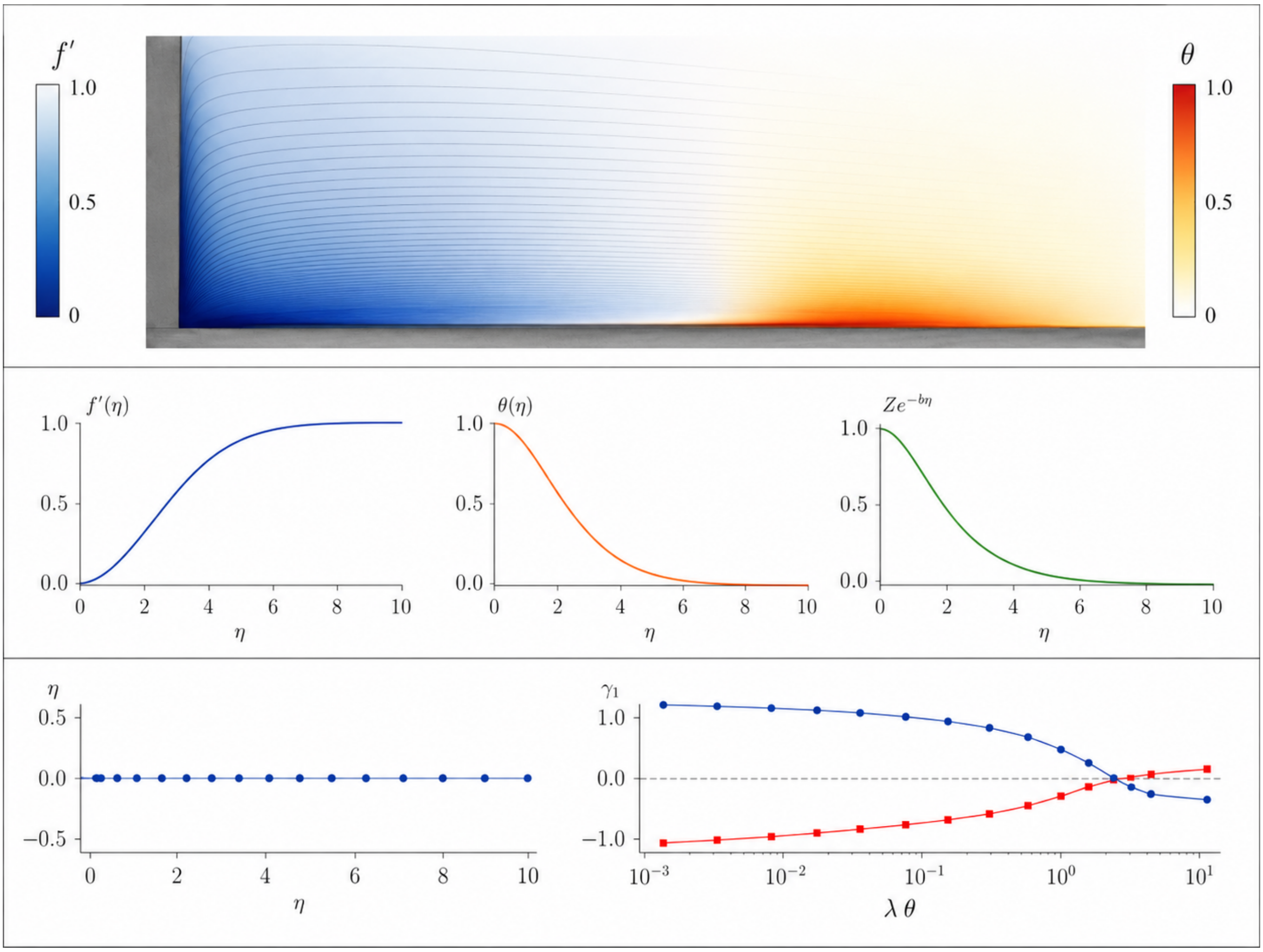

Figure 3: Similarity solution and stability pathway.

Table 2: Validation at $Pr = 0.72$, $\phi_{\mathrm{Cu}} = \phi_{\mathrm{Al_2O_3}} = 0$, $A = 0$, $R = 0$, and $Z = 0$; comparison values are cited in [29, 30].

Bi	Present $Re_x^{1/2}C_f$	Comparison $Re_x^{1/2}C_f$	Present $Re_x^{-1/2}Nu_x$	Comparison $Re_x^{-1/2}Nu_x$
0.05	1.2325876	1.2325877	0.045466	0.045466
0.10	1.2325876	1.2325877	0.083373	0.083373
0.20	1.2325876	1.2325877	0.142974	0.142974

5. Stability calculation and numerical method

Coupled nonlinear differential Eqs. (18) and (19) are reduced to first order and solved using a fourth-order collocation technique. Computational truncation occurs at $\eta_\infty = 10$, where $f'(\eta)$ reaches unity and $\theta(\eta)$ becomes negligible. Unless specified otherwise, we assume $Pr = 6.2$ and $\phi_{\mathrm{Cu}} = \phi_{\mathrm{Al_2O_3}} = 0.02$. The upper branch is obtained directly via the stability test, whereas the lower branch is computed by continuity in λ.

Limiting case of the viscous fluid can be obtained by setting $\phi_{\mathrm{Cu}} = \phi_{\mathrm{Al_2O_3}} = 0$, $A = 0$, $R = 0$, and $Z = 0$. For $Pr = 0.72$, we obtain $Re_x^{1/2}C_f = 1.2325876$, which matches the comparison value 1.2325877 reported in related convective-boundary-condition studies [29, 30]. The corresponding reduced Nusselt numbers are 0.045466, 0.083373, and 0.142974, when $Bi = 0.05$, 0.10, and 0.20, respectively. Those results are in agreement with the comparison values.

These values in Table 2 verify the solution of momentum and energy equations numerically. The skin friction coefficient is insensitive to variations in Bi since all other factors contributing to momentum (buoyancy force, thermal radiation, nanoparticles, and electromagnetism) are negligible in the limiting case of pure viscous fluid flow. The Nusselt number increases as Bi increases, implying that a larger convective wall heating results in steeper wall temperature gradients.

The results shown in Figure 4 demonstrate a monotonically increasing trend in the wall skin friction as the convective wall heating increases, similar to the tabulated data. It justifies the validity of the proposed method for the hybrid nanofluid simulations.

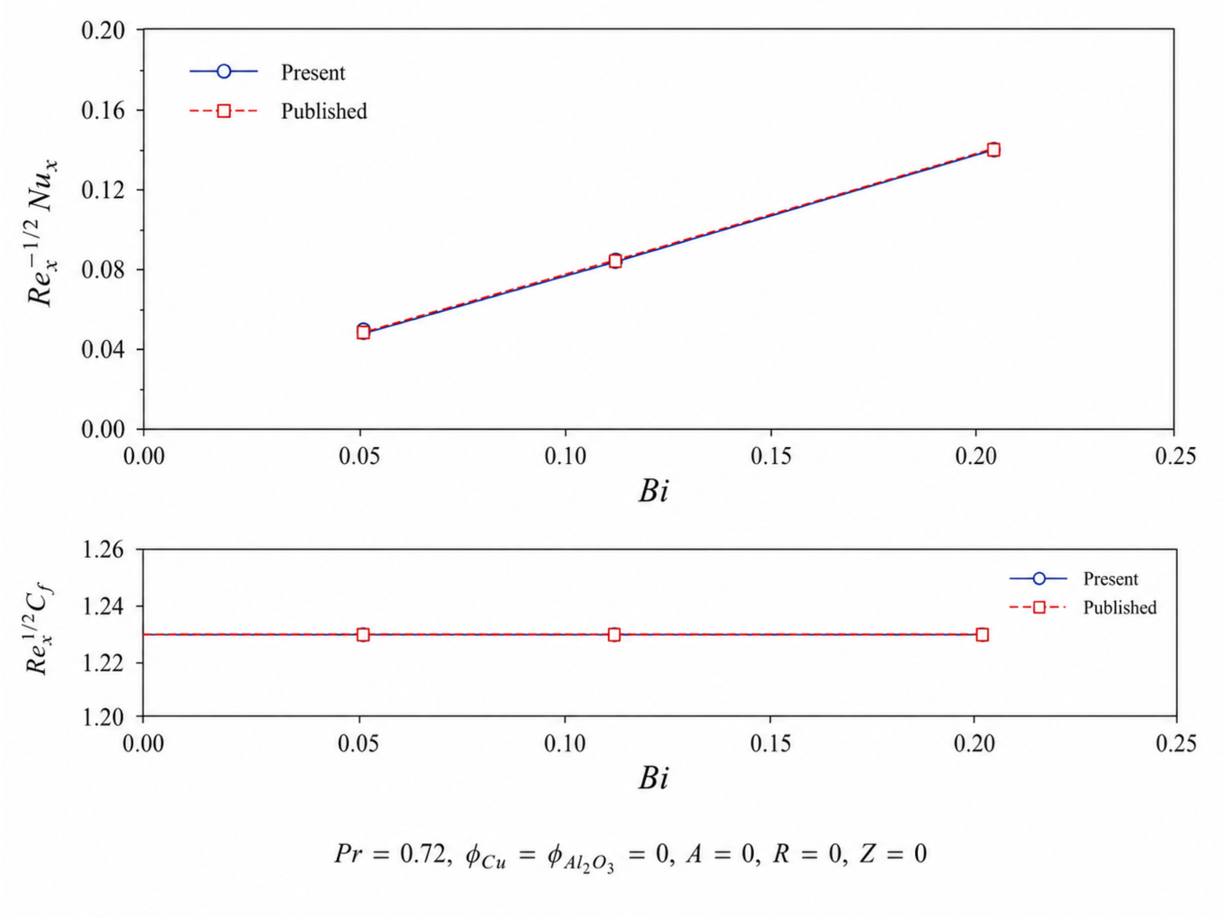

Figure 4: Verification of wall-gradient data.

For examining the temporal stability, we assume the dimensionless time dependence of the similarity functions,

$$u = \frac{ax}{1-ct}\frac{\partial f}{\partial \eta}(\eta,\tau), \qquad v = -\left(\frac{a\nu_{H_2O}}{1-ct}\right)^{1/2} f(\eta,\tau), \tag{32}$$

$$\theta(\eta,\tau) = \frac{T-T_\infty}{T_f(x,t)-T_\infty}. \tag{33}$$

The small-time perturbation can be written as

$$f(\eta,\tau) = f_0(\eta) + e^{-\gamma\tau}F(\eta), \qquad \theta(\eta,\tau) = \theta_0(\eta) + e^{-\gamma\tau}G(\eta), \tag{34}$$

where the subscript "0" denotes steady solutions. If $\gamma > 0$, the disturbance decays; conversely, $\gamma < 0$ means disturbance growth.

With this formulation, the linearized equations can be written as

$$\frac{\mu_{hnf}/\mu_{H_2O}}{\rho_{hnf}/\rho_{H_2O}}F''' + f_0F'' + Ff_0'' - 2f_0'F' - AF' - \frac{A}{2}\eta F'' + \frac{\beta_{hnf}}{\beta_{H_2O}}\lambda G + \gamma F' = 0, \tag{35}$$

$$\frac{1}{Pr}\frac{(\rho C_p)_{H_2O}}{(\rho C_p)_{hnf}}\left(\frac{k_{hnf}}{k_{H_2O}} + \frac{4R}{3}\right)G'' + f_0G' + F\theta_0' - \frac{A}{2}\eta G' + \gamma G = 0, \tag{36}$$

with the following boundary conditions:

$$F(0) = 0, \qquad F'(0) = 0, \qquad G'(0) = \frac{k_{H_2O}}{k_{hnf}}BiG(0),$$
$$F'(\eta) \to 0, \qquad G(\eta) \to 0 \qquad \text{as } \eta \to \infty. \tag{37}$$

They maintain the same wall and freestream properties but investigate the disturbance stability.

According to Table 3, the largest eigenvalues indicate the choice of the physical branch. The first branch has the eigenvalues greater than zero, while the second branch has negative eigenvalues. In other words, the upper branch is stable, but the lower branch is unstable.

Table 3: Eigenvalues for $Pr = 6.2$, $A = -0.5$, $\phi_{\mathrm{Al_2O_3}} = \phi_{\mathrm{Cu}} = 0.02$, $b = Z = Bi = 0.5$, and $R = 1.3$.

λ	First branch	Second branch
-1.0	0.97587	-1.51783
-0.5	1.86571	-1.78683
0.9	0.89239	-0.06152
1.0	0.88626	-0.06402

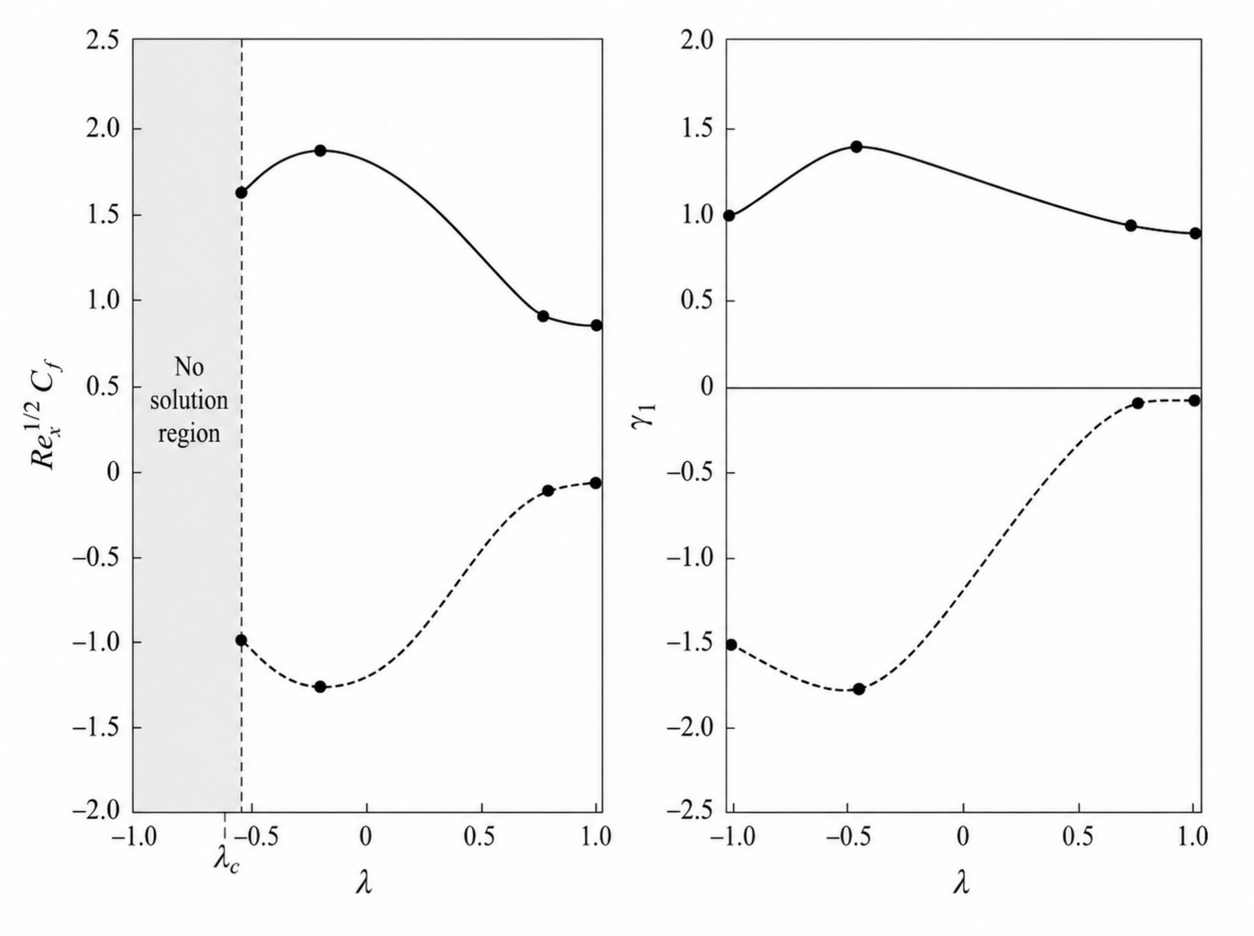

Figure 5: The branch stability based on eigenvalue analysis.

Figure 5 illustrates the stability issue through the graphical representation of the same decision. The solid branch is temporally admissible due to the positivity of the minimum eigenvalue, while the dashed branch falls below the neutral eigenvalue line and, hence, is unstable. The colored zone below depicts the region of non-admissible opposing flows.

6. Results and discussion

The transport performance is considered based on the skin-friction coefficient $Re_x^{1/2} C_f$, the Nusselt number $Re_x^{-1/2} Nu_x$, and the internal profiles responsible for producing these gradients on the walls. This combined reading is indispensable since any given enhancement in the heat-transfer coefficient might be caused by various mechanisms such as forced motion, assisting mixed convection, unsteady compression, enhanced wall heating, and radiative-conductive heat transfer. The temporal eigenvalue computation presented in Figure 5 serves as a stability criterion for the analysis; the physical branch corresponds to the first, while the second branch exists only to define the nonlinear structure of the BVP.

The value of λ defines whether the boundary layer admits a single or two mathematical states. Positive values of λ facilitate the stagnation flow field and provide a single-stable-state flow pattern. Negative values correspond to a flow that opposes the external stagnation stream, thus producing a dual solution within a finite range prior to reaching the critical value. The evidence shown in Figure 5 demonstrates that the lower branch is physically irrelevant despite the satisfaction of all steady boundary conditions. Such distinction is necessary as a wall-gradient value favorable at the lower branch will not be sustained under transient loading conditions.

The effect of unsteadiness A produces the most striking results in the present study. Figure 7 combines wall gradients of $A = -0.3$, -0.5, and -0.7 along with the stable flow profiles. The higher degree of decelerating unsteadiness lowers the

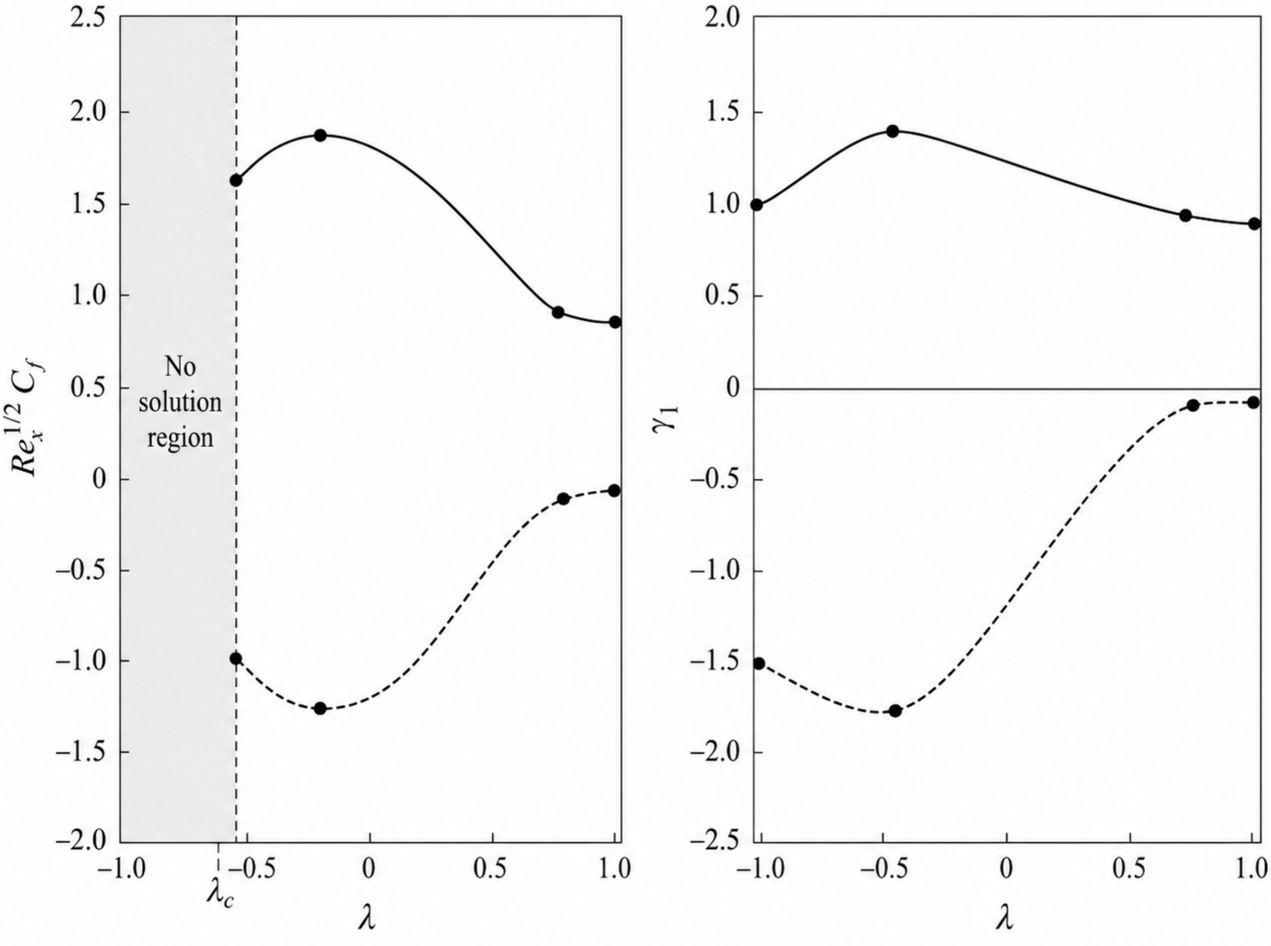

Figure 6: Admissible and non-admissible branches of eigenvalues in the plane.

skin-friction response while increasing the reduced Nusselt number. The reason for this trend can be seen from the velocity profiles: the greater value of $|A|$ decreases the near-wall velocity gradient as well as delays the asymptotic value of velocity. The thermal profile exhibits the inverse relation: the greater $|A|$ lowers the thickness of the thermal layer and steepens the wall temperature gradient.

Based on the results presented in Figure 7, it becomes clear that unsteadiness can act as a shear-temperature separator in the decelerating regime. The higher the magnitude of A, the less wall friction is developed while the greater the heat-extraction efficiency becomes. It should be noted that the conventional near-wall acceleration is accompanied by the simultaneous increase in heat transfer and shear, while here the former improves at the expense of the latter. However, the presented results remain valid only for the stable response; the lower branch does exist but it is physically irrelevant because of negative eigenvalues.

The parameter Z characterizes the intensity of the magnetic force applied by the Riga actuator. Figure 8 illustrates the response to the increase in this intensity by presenting the stable flow pattern for $Z = 0.5$, 1.0, and 1.5. As Z grows, the wall friction and heat transfer coefficients increase as well. The velocity profiles show why this happens: higher intensity of the magnetic force causes the near-wall acceleration that might result in a slight overshoot before the solution asymptotically reaches the free-stream value. On the other hand, the temperature profiles decrease as Z increases due to the enhanced near-wall cooling.

From Figure 8 it follows that the Riga actuator facilitates heat transfer via the coupling effect of momentum and thermal flows. The electromagnetic component operates directly in the momentum equation and indirectly via modified velocity in the energy equation. As a result, there is an improvement in the thermal response at the expense of increased wall shear. The latter occurs due to near-wall acceleration; accordingly, it should be taken into account during design optimization. The optimal value of Z is not the highest available one because of this trade-off.

Parameter b determines how far the electromagnetic field penetrates into the boundary layer. Figure 9 reveals a clear trend in wall shear and thermal responses in the case of positive Lorentz force. With increasing b, both the skin friction and heat transfer coefficients drop since electromagnetic forcing acts in a narrower region close to the wall surface. In addition, the field-penetration plot shown on the left illustrates the physical meaning of the parameter.

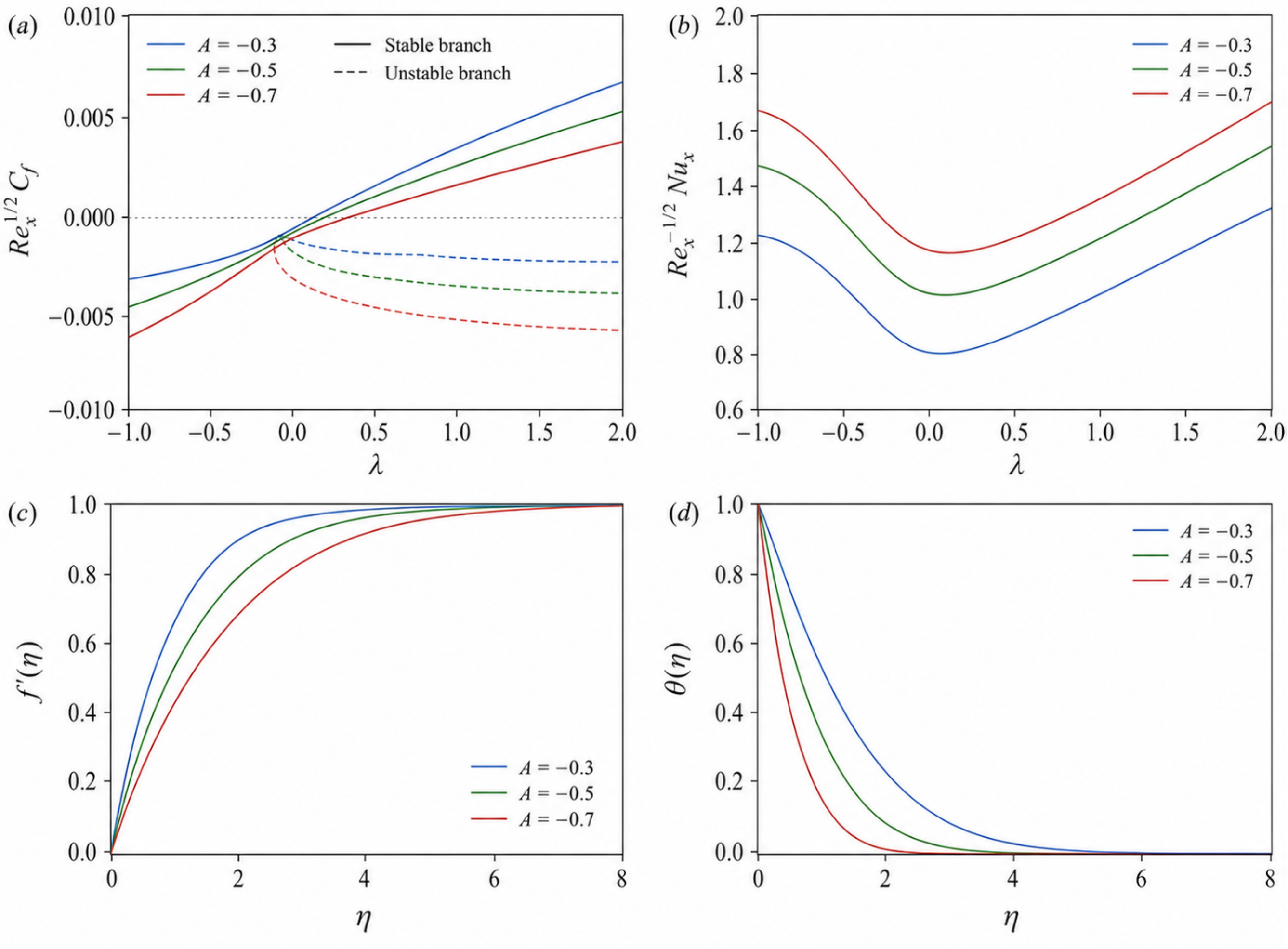

Figure 7: Unsteadiness response of wall gradients and profiles.

Thus, the results illustrated in Figure 9 demonstrate the need for combining the parameters Z and b. While the former parameter determines the intensity of the magnetic force, the latter defines the penetration into the boundary layer. A force with a high intensity acting in a small volume might not result in the same level of heat extraction as a less intense force affecting a broader region. Moreover, the reduced penetration depth may help reduce wall shear when it is required.

Mixed convection parameter modifies the flow by introducing an additional buoyancy effect. Figure 10 compares the steady velocity and temperature profiles for the cases of $\lambda = -0.5$, 0.5, and 1.0. An increase in λ leads to the elevation of the wall velocity gradient due to the assisting effect of the buoyancy. Simultaneously, thermal layer gets thinned while heat transfer gets improved; otherwise, the opposing mixed convection results in the approach to dual solutions.

Based on the evidence illustrated in Figure 10, it can be said that the effect of λ can be characterized by increased wall velocity gradient and the decrease of the thermal thickness. As a result, heat transfer gets improved but with the corresponding shear penalty. At the same time, the decelerating unsteadiness results in higher heat transfer without any shear penalty. The latter distinction is crucial since only this mechanism can help improve heat transfer while reducing wall friction simultaneously.

Biot number acts in the current problem by modifying the thermal condition at the walls. As seen in Figure 11, an increase in the value of Bi from 0.3 to 0.7 increases the temperature distribution. This happens due to the enhanced thermal communication between the heated external fluid and the hybrid nanofluid. It should be mentioned that the side notation in Figure 11 describes the role of radiation in the system through the combined parameter $k_{hnf}/k_{H_2O} + 4R/3$. It affects the value of the temperature gradient in the Nusselt number.

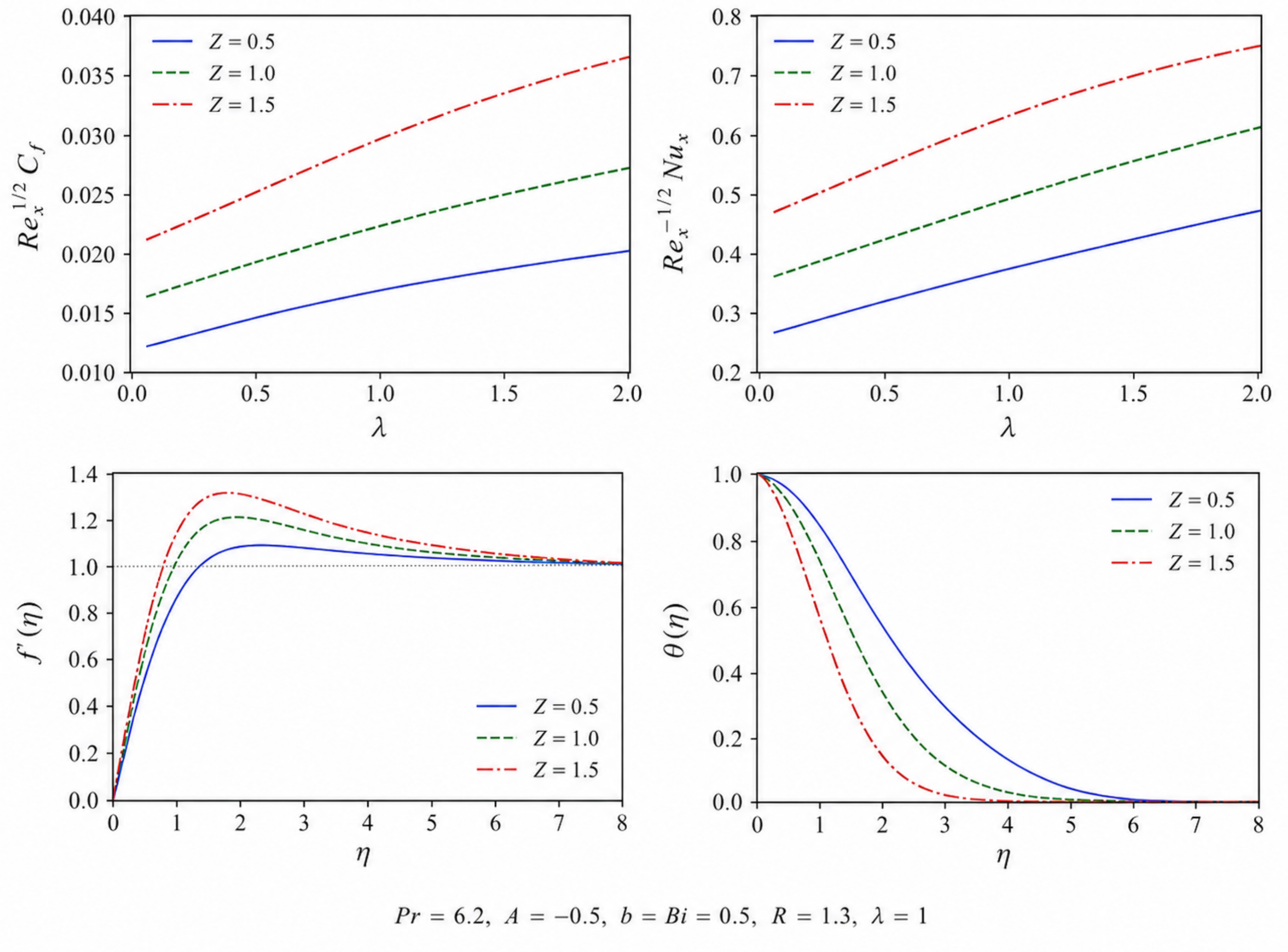

Figure 8: Riga-force intensity response.

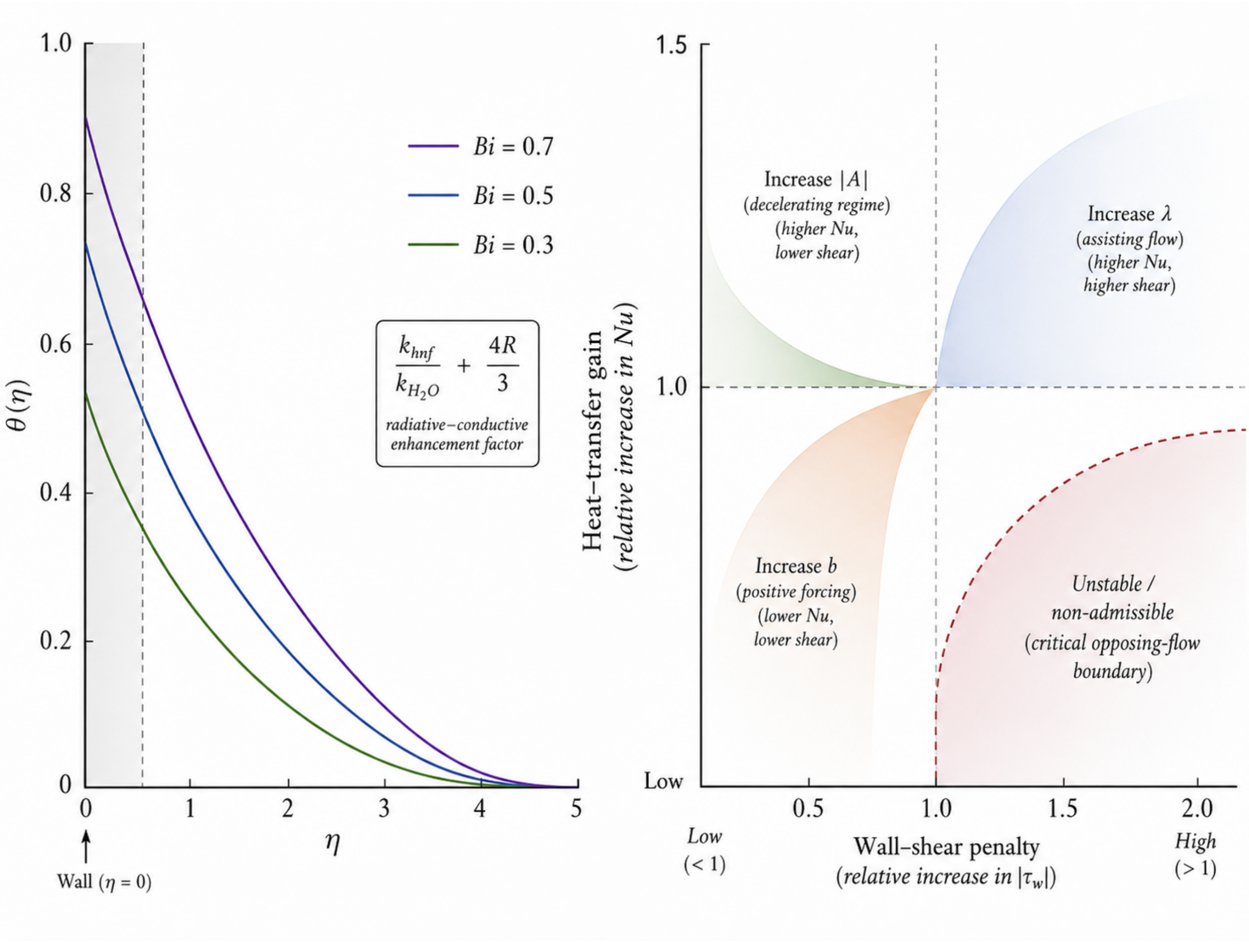

Figure 11: Wall heating and stable operating map.

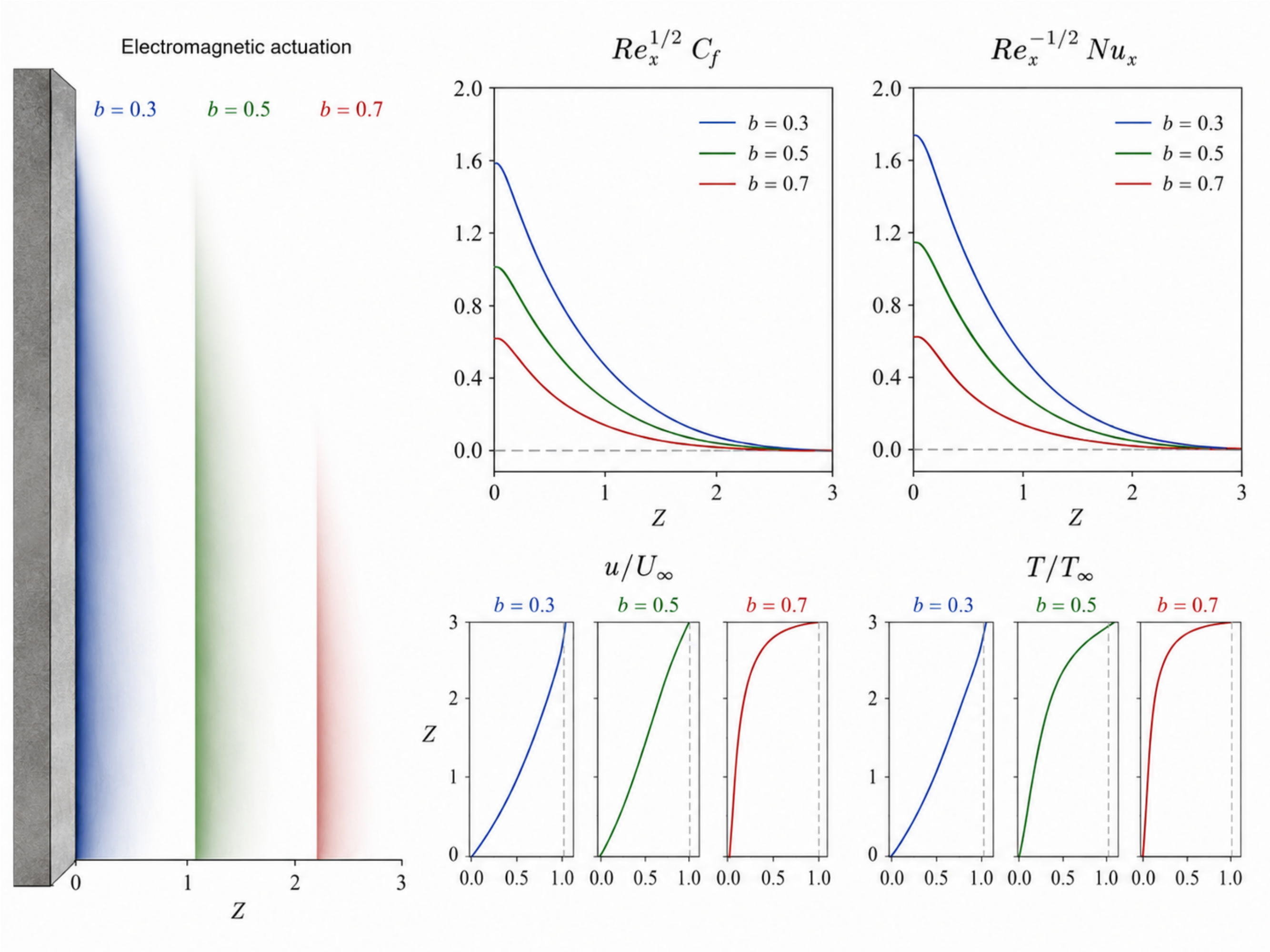

Figure 9: Electromagnetic decay and penetration.

An analysis of the operating map illustrated in Figure 11 allows one to formulate several conclusions about the transport response of the system. First, the increase in Z and assisting λ leads to higher heat transfer and wall friction coefficients. Second, an increase in $|A|$ for decelerating unsteadiness promotes higher heat transfer while reducing wall friction. Third, positive electromagnetic force with an increasing value of b decreases the heat transfer while lowering the friction coefficient. The non-admissible region colored in blue reflects the requirement to maintain the physical admissibility. Thus, a feasible operating state should be selected on the stable branch, provide an improvement in heat transfer, and be free from shear penalty.

Concluding, one can say that the considered Cu–Al_2O_3/water nanofluid system cannot be investigated based on the heat-transfer characteristics alone. The copper additive enhances the conductive properties of the hybrid suspension, whereas aluminum oxide provides the ceramic component. In addition, water preserves the high heat capacity of the carrier liquid. Coupled with the effects of viscosity, density, thermal storage, and buoyancy, the material properties of the considered fluid system result in the fact that a higher Nusselt number requires the corresponding response in the wall shear coefficient. The first branch, the moderate extent of electromagnetic field, and the controlled wall shear constitute the physical domain of validity for the Riga-driven hybrid nanofluid boundary-layer problem.

7. Conclusions

An analysis of the unsteady mixed-convection flow of a Cu–Al_2O_3/water hybrid nanofluid over a fixed vertical Riga plate under convective wall heating has been carried out. The proposed mathematical model includes the effective fluid properties of the Cu–Al_2O_3/water fluid mixture, the exponentially decaying Grinberg Lorentz force, Rosseland radiation model, unsteady stagnation velocity, and buoyancy force. A similarity formulation leads to the governing nonlinear boundary value problem, which is solved numerically by the fourth-order Runge-Kutta collocation approach. The temporal stability analysis reveals the stable and unstable branches of solutions.

The viscous-fluid computation is used to validate the numerical scheme. When $Pr = 0.72$, $A = R = Z = 0$, and there is zero volume fraction of nanoparticles, the computation yields $Re_x^{1/2} C_f = 1.2325876$ and $Re_x^{-1/2} Nu_x = 0.045466$, 0.083373,

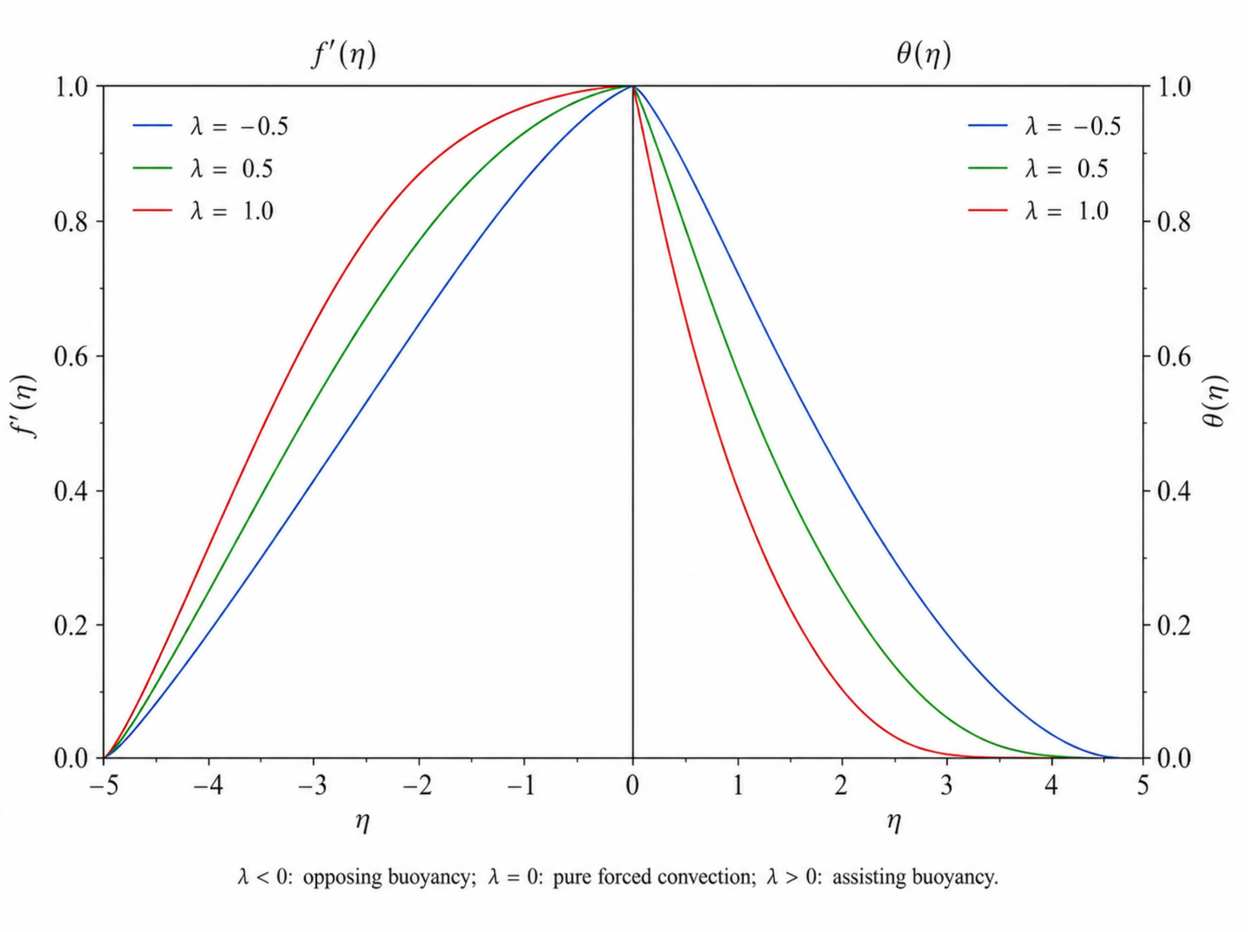

Figure 10: Buoyancy effect on velocity and temperature profiles.

and 0.142974 when $Bi = 0.05$, 0.10, and 0.20. Comparison with other results ensures the validity of the momentum equation, energy equation, and convective wall boundary condition.

The sign of the mixed-convection parameter determines the existence and stability of the solution. Assisted flow admits one stable branch only. However, opposition admits two branches until a certain critical point is reached. Positive eigenvalues are associated with the first branch, whereas negative eigenvalues describe the second branch. Hence, physical considerations must focus on the first branch.

Unsteady deceleration generates the best combination response among the investigated parameters. As $|A|$ grows, the near-wall velocity distribution becomes weaker, leading to the lowering of the reduced skin-friction coefficient, the lowering of temperature profile, the increase in the wall temperature gradient, and the raising of reduced Nusselt number. In conclusion, unsteadiness may reduce the mechanical loadings while enhancing heat transfer.

The modified Hartmann number increases the electromagnetic acceleration in the near-wall region. Higher values of Z mean higher velocity gradient at the wall, skin friction, compression of the thermal boundary layer, and enhanced Nusselt number. On the contrary, the decay parameter b acts negatively on the Lorentz force; hence, higher values result in the restriction of the Lorentz force to a smaller region, reduction in the velocity enhancement, as well as wall shear and heat transfer.

Assisted buoyancy causes higher velocities in the stable solution and better heat transfer but higher wall shear as well. The convective wall heating affects the solution via the imposed boundary condition; therefore, higher values of Bi increase temperature distribution by enhancing the thermal communication between the heated fluid and hybrid nanofluid. Radiation has an impact via the effective thermal diffusivity factor and should be understood jointly with the hybrid thermal conductivity. The transport of Cu–Al_2O_3/water near a vertical Riga plate under assisting buoyancy is controlled by the proper choice of A, λ, Z, b, Bi, and R.

Conflict of interest

The author declared no conflict of interest.

References

[1] Choi, S. U. (1995, November). Enhancing thermal conductivity of fluids with nanoparticles. In ASME international mechanical engineering congress and exposition (Vol. 17421, pp. 99-105). American Society of Mechanical Engineers.

[2] Eastman, J. A., Choi, S. U. S., Li, S., Yu, W., & Thompson, L. J. (2001). Anomalously increased effective thermal conductivities of ethylene glycol-based nanofluids containing copper nanoparticles. Applied physics letters, 78(6), 718-720.

[3] Buongiorno, J. (2006). Convective transport in nanofluids.

[4] Tiwari, R. K., & Das, M. K. (2007). Heat transfer augmentation in a two-sided lid-driven differentially heated square cavity utilizing nanofluids. International Journal of heat and Mass transfer, 50(9-10), 2002-2018.

[5] Kakaç, S., & Pramuanjaroenkij, A. (2009). Review of convective heat transfer enhancement with nanofluids. International journal of heat and mass transfer, 52(13-14), 3187-3196.

[6] Mahian, O., Kolsi, L., Amani, M., Estellé, P., Ahmadi, G., Kleinstreuer, C., ... & Pop, I. (2019). Recent advances in modeling and simulation of nanofluid flows-Part I: Fundamentals and theory. Physics reports, 790, 1-48.

[7] Sarkar, J., Ghosh, P., & Adil, A. (2015). A review on hybrid nanofluids: recent research, development and applications. Renewable and Sustainable Energy Reviews, 43, 164-177.

[8] Sidik, N. A. C., Adamu, I. M., Jamil, M. M., Kefayati, G. H. R., Mamat, R., & Najafi, G. (2016). Recent progress on hybrid nanofluids in heat transfer applications: a comprehensive review. International communications in heat and mass Transfer, 78, 68-79.

[9] Babu, J. R., Kumar, K. K., & Rao, S. S. (2017). State-of-art review on hybrid nanofluids. Renewable and Sustainable Energy Reviews, 77, 551-565.

[10] Suresh, S., Venkitaraj, K. P., Selvakumar, P., & Chandrasekar, M. (2011). Synthesis of Al2O3–Cu/water hybrid nanofluids using two step method and its thermo physical properties. Colloids and Surfaces A: Physicochemical and Engineering Aspects, 388(1-3), 41-48.

[11] Takabi, B., & Salehi, S. (2014). Augmentation of the heat transfer performance of a sinusoidal corrugated enclosure by employing hybrid nanofluid. Advances in Mechanical Engineering, 6, 147059.

[12] Devi, S. A., & Devi, S. S. U. (2016). Numerical investigation of hydromagnetic hybrid Cu–Al2O3/water nanofluid flow over a permeable stretching sheet with suction. International Journal of Nonlinear Sciences and Numerical Simulation, 17(5), 249-257.

[13] Goldstein, S. (1965). On backward boundary layers and flow in converging passages. Journal of Fluid Mechanics, 21(1), 33-45.

[14] Merkin, J. H. (1986). On dual solutions occurring in mixed convection in a porous medium. Journal of engineering Mathematics, 20(2), 171-179.

[15] Weidman, P. D., Kubitschek, D. G., & Davis, A. M. J. (2006). The effect of transpiration on self-similar boundary layer flow over moving surfaces. International journal of engineering science, 44(11-12), 730-737.

[16] Gailitis, A. (1961). On a possibility to reduce the hydrodynamical resistance of a plate in an electrolyte. Appl. Magnetohydrodyn., 12, 143-146.

[17] Grinberg, E. (1961). On determination of properties of some potential fields. Appl. Magnetohydrodyn. Rep. Phys. Inst. Riga, 12, 147-154.

[18] Pantokratoras, A., & Magyari, E. (2009). EMHD free-convection boundary-layer flow from a Riga-plate. Journal of engineering mathematics, 64(3), 303-315.

[19] Magyari, E., & Pantokratoras, A. (2011). Aiding and opposing mixed convection flows over the Riga-plate. Communications in Nonlinear Science and Numerical Simulation, 16(8), 3158-3167.

[20] Bhatti, M. M., Abbas, T., & Rashidi, M. M. (2016). Effects of thermal radiation and electromagnetohydrodynamics on viscous nanofluid through a Riga plate. Multidiscipline Modeling in Materials and Structures, 12(4), 605-618.

[21] Ayub, M., Abbas, T., & Bhatti, M. M. (2016). Inspiration of slip effects on electromagnetohydrodynamics (EMHD) nanofluid flow through a horizontal Riga plate. The European Physical Journal Plus, 131(6), 193.

[22] Ahmad, R., Mustafa, M., & Turkyilmazoglu, M. (2017). Buoyancy effects on nanofluid flow past a convectively heated vertical Riga-plate: A numerical study. International Journal of Heat and Mass Transfer, 111, 827-835.

[23] Khashi'ie, N. S., Md Arifin, N., & Pop, I. (2020). Mixed convective stagnation point flow towards a vertical Riga plate in hybrid Cu-Al2O3/water nanofluid. Mathematics, 8(6), 912.

[24] Zainal, N. A., Nazar, R., Naganthran, K., & Pop, I. (2020). Unsteady stagnation point flow of hybrid nanofluid past a convectively heated stretching/shrinking sheet with velocity slip. Mathematics, 8(10), 1649.

[25] Khatun, S., Islam, M. M., Mollah, M. T., Poddar, S., & Alam, M. M. (2021). EMHD radiating fluid flow along a vertical Riga plate with suction in a rotating system. SN Applied Sciences, 3(4), 452.

[26] Khashi'ie, N. S., Arifin, N. M., Sheremet, M., & Pop, I. (2021). Shape factor effect of radiative Cu–Al2O3/H2O hybrid nanofluid flow towards an EMHD plate. Case Studies in Thermal Engineering, 26, 101199.

[27] Wahid, N. S., Arifin, N. M., Khashi'ie, N. S., Pop, I., Bachok, N., & Hafidzuddin, M. E. H. (2022). Hybrid nanofluid stagnation point flow past a slip shrinking Riga plate. Chinese Journal of Physics, 78, 180-193.

[28] Ramzan, M., Javed, M., Rehman, S., Ahmed, D., Saeed, A., & Kumam, P. (2022). Computational assessment of microrotation and buoyancy effects on the stagnation point flow of carreau–yasuda hybrid nanofluid with chemical reaction past a convectively heated riga plate. ACS omega, 7(34), 30297-30312.

[29] Saleh, S. H. M., Arifin, N. M., Nazar, R., Ali, F. M., & Pop, I. (2014). Mixed convection stagnation flow towards a vertical shrinking sheet. International Journal of Heat and Mass Transfer, 73, 839-848.

[30] Mohamed, M. K. A., Salleh, M. Z., Ishak, A., & Pop, I. (2015). Stagnation point flow and heat transfer over a stretching/shrinking sheet in a viscoelastic fluid with convective boundary condition and partial slip velocity. The European Physical Journal Plus, 130(8), 171.

[31] Rosseland, S. (1936). Theoretical Astrophysics, Oxford University Press. London).